coatings

MDPI

Article

Microstructure, Texture and Mechanical Properties of Al-SiC Composite with Bimodal Structure Fabricated by Multi-Layer Accumulative Roll Bonding

Shengcheng Zhang *, Liqun Wei *, Bin Fu and Yanhui Guo

School of Materials Science and Engineering, Shanghai Institute of Technology, Shanghai 201418, China
* Correspondence: 206081130@mail.sit.edu.cn (S.Z.); weiliqun@sit.edu.cn (L.W.)

Abstract: A multi-layer accumulative roll bonding (MARB) process was applied to fabricate Al-1 vol% SiC composite (M3) with bimodal structure consisting of 1.07 μm ultrafine grain layers and 0.48 μm finer grain layers. The differences in microstructure, texture and mechanical properties of the M3 samples were systematically compared with conventional MARB-processed Al (M1) and bimodal Al (M2) samples. Optical microscopy (OM), scanning electron microscopy (SEM) and electron backscatter diffraction (EBSD) analysis were used to characterize the microstructure evolution of the composites, while the mechanical properties were analyzed by tensile and microhardness tests. As revealed by EBSD results after three cycles, the M3 samples had a bimodal grain structure of 0.48 and 1.07 μm. The texture components of the M3 samples were Brass {011} <211>, S {123} <634>, Cube {001} <100> and Copper {112} <111>. According to SEM observation, ductile fracture of M3 was characterized by acicular dimple and circular micropores. Bimodal Al-SiC composites with high strength (225 MPa) and elongation (13%) were finally synthesized after three cycles. Compared with M1 sheets, the strength and elongation of the M3 sheets increased by 23.2% and 7.4%, respectively, indicating that the M3 samples achieved a synergistic improvement in strength and plasticity.

Keywords: accumulative roll bonding; aluminum matrix composites; bimodal grain structure; mechanical properties

check for updates

Citation: Zhang, S.; Wei, L.; Fu, B.; Guo, Y. Microstructure, Texture and Mechanical Properties of Al-SiC Composite with Bimodal Structure Fabricated by Multi-Layer Accumulative Roll Bonding. *Coatings* **2023**, *13*, 512. https://doi.org/10.3390/coatings13030512

Academic Editor: Aivaras Kareiva

Received: 31 January 2023
Revised: 18 February 2023
Accepted: 23 February 2023
Published: 25 February 2023

Copyright: © 2023 by the authors. Licensee MDPI, Basel, Switzerland. This article is an open access article distributed under the terms and conditions of the Creative Commons Attribution (CC BY) license (https://creativecommons.org/licenses/by/4.0/).

1. Introduction

High strength and ductility are the primary objectives to achieve for the research and development of structural materials. The external properties of the materials reflect the characteristics of their microstructure, and the grain size is a major factor that affects the mechanical properties of metal materials. Therefore, ultrafine and nanocrystalline materials have attracted extensive attention in recent years [1–4]. In the process of severe plastic deformation (SPD), a large strain is applied at the original grain scale of the material to effectively refine the coarse-grained (CG) microstructures into ultrafine-grained (UFG) or even nanocrystalline microstructures. It does not cause any significant change to the overall material dimensions or lead to impurities and micropores. The mainstream SPD techniques include accumulative roll bonding (ARB) [5–8], equal-channel angular pressing (ECAP) [9] and high-pressure torsion (HPT) [10,11]. Among them, ARB is one of the most promising and cost-effective solutions to the continuous preparation of ultrafine metal sheets [12,13].

The major challenges in preparing the materials with both high strength and ductility through ARB are technological limitations and the match of strength and plasticity. In order to design and develop aluminum alloys with an excellent combination of strength and ductility, it is urgent to design the material microstructure and improve the ARB process. The fabrication of metal matrix composites (MMCs) is an effective way to further increase strength and hardness [14–18]. However, it has been demonstrated that the production of MMCs by the ARB method requires a larger extent of rolling reduction and strain. [19,20]. The conventional ARB process means two-layer rolling in a cycle, so the newly formed

interface in the previous pass often causes poor bonding, and the accumulation of strain is low in efficiency. Therefore, the ARB process has been improved and optimized to multi-layer accumulative roll bonding (MARB) [21,22]. In addition to improving the efficiency of strain accumulation and making the interface bond well, the MARB technique also promotes the uniform distribution of ceramic particles within the metal matrix.

Achieving reasonable ductility in MMCs with high strength and hardness is a challenge. As a mix of micron-sized and submicron/nanocrystalline grains, the bimodal structure is effective in preventing premature local plastic deformation [23–26]. The micron-sized grains have strain hardening capability and can be used to delay the local plastic deformation of materials, which is conducive to the uniform elongation of the materials [27,28]. Based on the further investigation of the literature, the uniform elongation may suddenly drop in the aluminum alloys by decreasing the deformed grain size below 1 μm in the normal direction (ND) [29]. It is possible to control grain size by intermediate annealing in a single MARB cycle. This study attempts to fill the research gap concerning the preparation of MMCs with bimodal grain structure (below and above 1 μm).

In conclusion, the objective of producing bimodal structured Al-SiC composites (short as M3) by the MARB process is to obtain favorable properties, and also to investigate the evolution pattern of microstructure and mechanical properties of the samples under MARB passes. To manifest the advantages of the M3 samples, there are two groups of samples designed: Al (short as M1) and bimodal Al (short as M2) sheets prepared by the MARB process.

2. Materials and Methods

2.1. Materials

The experimental material used in the study was 1050 plate, sized 100 mm × 30 mm × 1 mm. The chemical composition of the samples is detailed in Table 1 and the SEM of SiC ceramic particles is shown in Figure 1a. The SEM instrument was the Zeiss Gemini 300 (Oberkochen, Germany). The average particle size (APS) of SiC was about 3.09 μm, which is shown in Figure 1b. The sheets were annealed at 500 °C for 2 h and cooled in air, with the layers of annealed plates (short as L1) whose grain structure is shown in Figure 1c. The average grain size (AGS) of the annealed Al sheet was about 31 μm, which is shown in Figure 1d.

Table 1. Chemical composition of 1050 Al.

Element	Al	Si	Ti	Fe	Others
Wt.%	99.61	0.08	0.013	0.26	0.37

2.2. MARB Process

All plates were scraped and polished with a stainless-steel brush (100 mm in circumferential diameter, 0.3 mm in wire diameter and 2000 rpm) before MARB to ensure the purity and roughness of the surfaces. Subsequently, the sheet was washed with acetone and dried in air. The MARB process was accomplished on the rolling mill with a 180 mm diameter at the rotational speed of 25 rpm.

The major links of roll bonding are shown in Figure 2. In step 1, the experimental sheets of M1, M2 and M3 were prepared. All samples were stacked using nylon ties to avoid defects. The two annealed plates were roll-bonded with 50% reduction to obtain one pass plates and the layers of them were denoted as L2. Sample M1 consisted of four annealed sheets, while sample M2 consisted of two annealed core-sheets and two one-pass outer-sheets. The difference between M3 and M2 was that the M3 samples had a total of 1 vol% SiC particles uniformly distributed between the plates. In step 2, the fixed four-layer sample plate was rolled with a 50% reduction. Subsequently, the sheets were annealed at 200 °C for 10 min. Then, they were rolled again with 50% reduction to obtain the first-cycle sample. After removal of cracks on the sample plate's edge, it was equally divided into

four pieces, brushed and polished. Finally, the process of step 2 was repeated until the total MARB process reached 4 cycles.

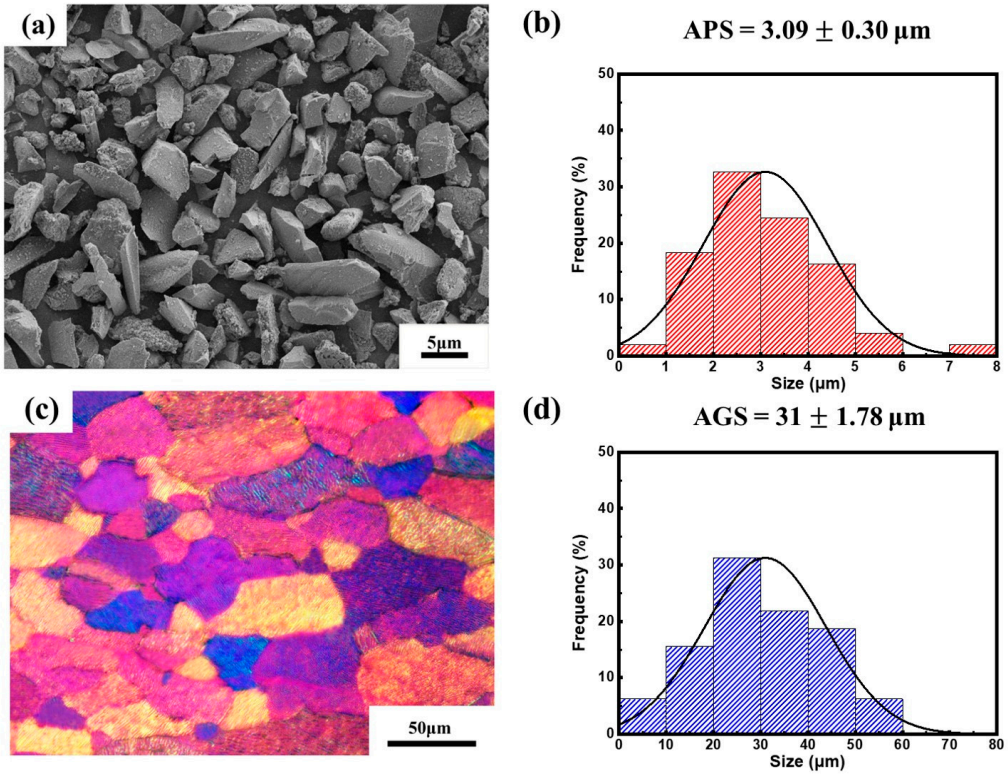


Figure 1. (**a**) SEM image of micron-sized SiC particles; (**b**) APS distribution of SiC particles; (**c**) optical micrograph of annealed 1050 Al; (**d**) AGS distribution of annealed 1050 Al.

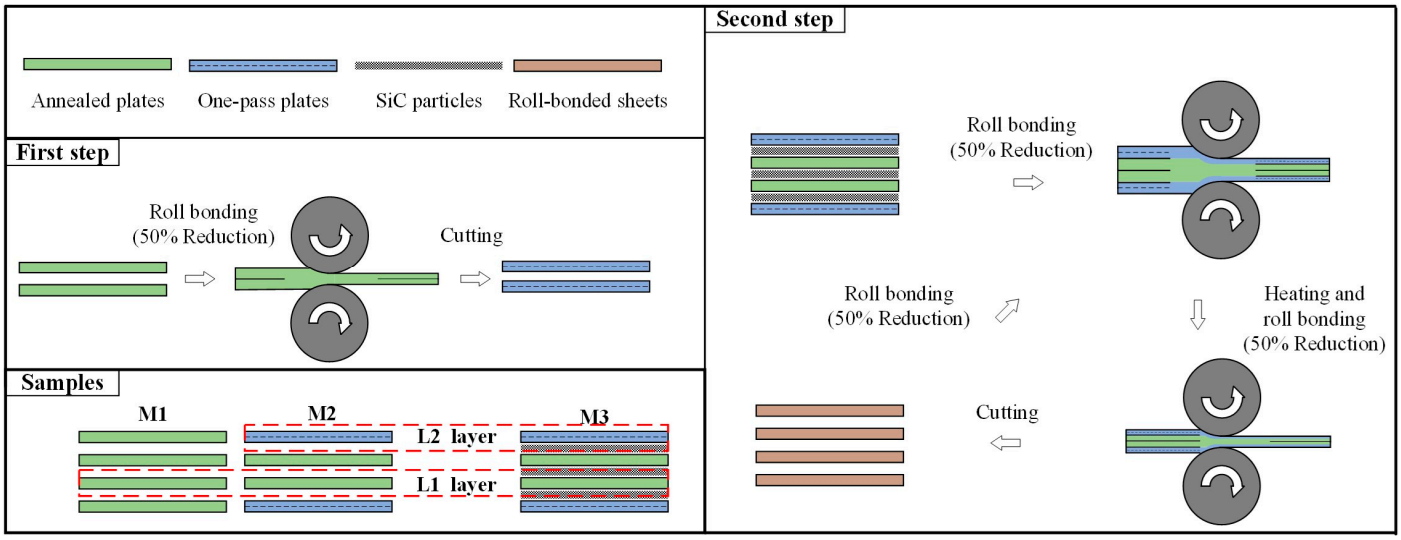


Figure 2. Schematic illustration of producing M1, M2 and M3 samples by the MARB process and illustration of L1 and L2 layers.

2.3. Microstructure

The microstructures of the sample after different MARB passes were characterized by OM, SEM and EBSD. The annealed Al samples were anodized with 10 wt.% HBF_4 aqueous solution at voltage 25 V and current 0.2 A for 60 s to observe the features of the grain. The OM, SEM and EBSD instruments were the Zeiss Axio D1M (Oberkochen, Germany),

the Zeiss Gemini 300 (Oberkochen, Germany) and the EDAX-TSL (Berwyn, PA, USA), respectively. The specimens used for EBSD were polished on a rolling direction–normal direction (RD–ND) surface with 2000# sandpaper and subsequently polished with a 0.5 μm diamond paste at 900 rpm speed. Then, samples were electrochemically polished in a mixture of 900 mL CH_3 OH and 100 mL $HClO_4$. Electropolish was performed at −30 °C and 20 v about 20 s. The EBSD data were analyzed by using TSL OIM 7.3 analysis software.

2.4. Mechanical Properties

Vickers hardness tests were performed using the 402SXV hardness tester (Shanghai, China) at room temperature on specimens of different passes in the RD–ND plane under a load of 100 g for 20 s. Tensile specimens were prepared along the rolling dimension by a wire-cut electric discharge machine, as shown in Figure 3. SANS-CMT5305 tensile test machine (St.Paul, MN, USA) was used with an initial strain rate of 1 mm/min, according to ASTM E8 M−11. The mechanical tests were repeated at least three times to verify the accuracy of the results.

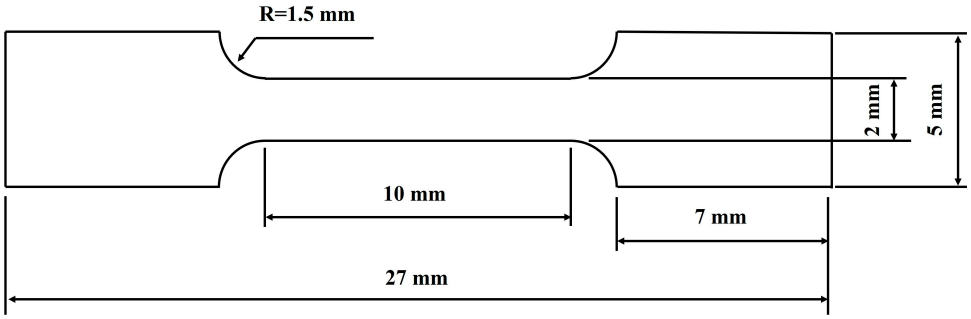


Figure 3. Schematic of the tensile-test samples.

3. Results

3.1. Microstructure Evolution

Figure 4 shows the OM images of bonding interfaces in M3 after the third and fourth cycle of the MARB process. Micron-sized SiC particles in the M3 samples dispersed between the interfaces of plate layers (Figure 4a,b). As the number of MARB cycles increased, the plastic flow of Al matrix promoted the SiC particles to gradually diffuse from the cluster area to the surrounding area, and finally distributed uniformly in the matrix (Figure 4a,b). The MARB way was effective in improving the bonding condition of the interface, so the Al layers of the M3 samples were firmly bonded and the boundary between layers could not be distinguished after the third cycle (Figure 4a). The bonding interface of the Al layers consisted of large, uniformly distributed SiC particles and a few particle-free zones (Figure 4a). The SiC particles were basically uniformly distributed in the Al matrix (Figure 4a), which indicated that the Al-1 vol%SiC composite with a uniformly distributed hard phase was prepared successfully after three MARB cycles.

Figure 5 shows the EBSD (IPF + GB) of M1 (Figure 5a), M2 (Figure 5b,d) and M3 (Figure 5c,e) after three MARB cycles. The thick black line indicates a high-angle grain boundary (HAGB), while the thick white line indicates a low-angle grain boundary (LAGB). L1 layers (Figure 5a,d,e) were dominated by the grains elongated along the RD, and L2 layers (Figure 5b,c) were dominated by the thinner grains along the RD. Some recrystallized grains were also observed at the grain boundaries. Figure 6 shows the AGS distribution in the M2 and M3 samples. The AGS in the ND of the L1 layers in M1 (Figure 5a), M2 (Figures 5d and 6a) and M3 (Figures 5e and 6b) were 0.92, 1.15 and 1.07 μm, while that of the L2 layers of M2 (Figures 5b and 6a) and M3 (Figures 5c and 6b) were 0.46 and 0.48 μm. There, the AGS of L1 layers and L2 layers had about a two-fold relationship in size to that of ND. Thus, the grain size of the L2 layers was smaller than 1 μm and that of the L1 layers was larger than 1 μm after three MARB passes. The AGS in the RD of the L1 layers in M1

(Figure 5a), M2 (Figures 5d and 6a) and M3 (Figure 5e) were 2.81, 2.75 and 2.68 μm, while that of the L2 layers in M2 (Figure 5b) and M3 (Figure 5c) were 1.52 and 1.58 μm. The grain axial ratio of the L1 layers in M1 (Figure 5a), M2 (Figures 5d and 6a) and M3 (Figure 5e) were 3.05, 2.39 and 2.5, while that of the L2 layers in M2 (Figure 5b) and M3 (Figure 5c) were 3.3 and 3.29.

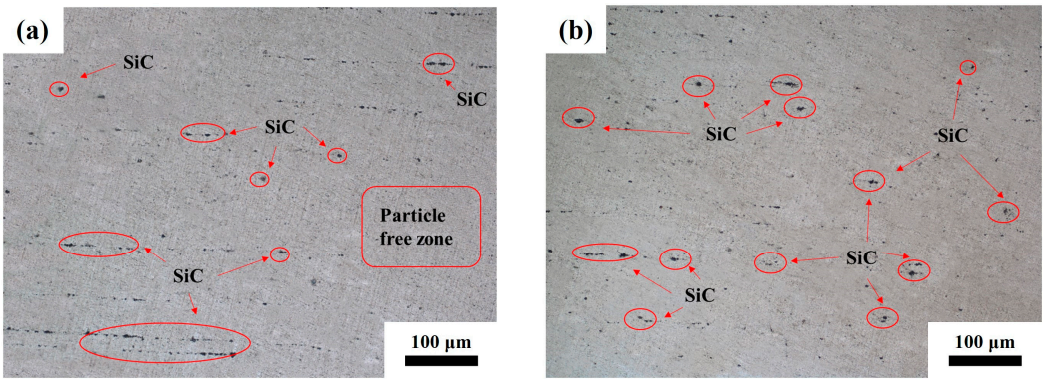


Figure 4. Optical micrographs of the bonding interfaces in the M3 samples after three (**a**) and four (**b**) MARB cycles.

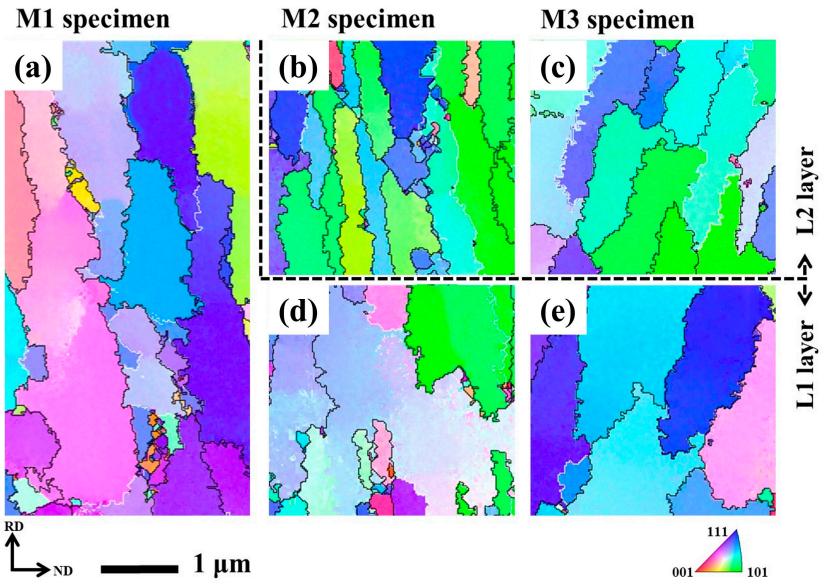


Figure 5. EBSD map of (**a**) M1, (**b**,**d**) M2 and (**c**,**e**) M3 sheets after three MARB cycles.

Figure 7 demonstrates the {111} pole figures (PFs) for the M1 (Figure 7a), M2 (Figure 7b) and M3 (Figure 7c) samples after three cycles. The positions of ideal orientation for the Cube {001} <100>, Goss {011} <001>, Brass {011} <211>, S {123} <634> and Copper {112} <111> texture components were marked in the {111} PFs [30,31]. It was observed that in the M1 (Figure 6a) specimen, the main texture components were the S {123} <634> component with an intensity of 2.1 × R, and the weak texture showing in M1 were Cube {001} <100> and Brass {011} <211> with an intensity of 1.6 × R and 1.2 × R. In the case of the M2 samples (Figure 7b), the main texture components were Brass {011} <211> and S {123} <634> with a maximum intensity of 5.5 × R and 2.4 × R. A weak Cube {001} <100> texture component was also present in the M2 samples with an intensity of 1.2 × R. The texture components of the M3 samples (Figure 7c) could be characterized as Brass {011} <211>, S {123} <634> and Cube {001} <100> with a maximum intensity of 3.8 × R, 2.2 × R and 1.3 × R, respectively.

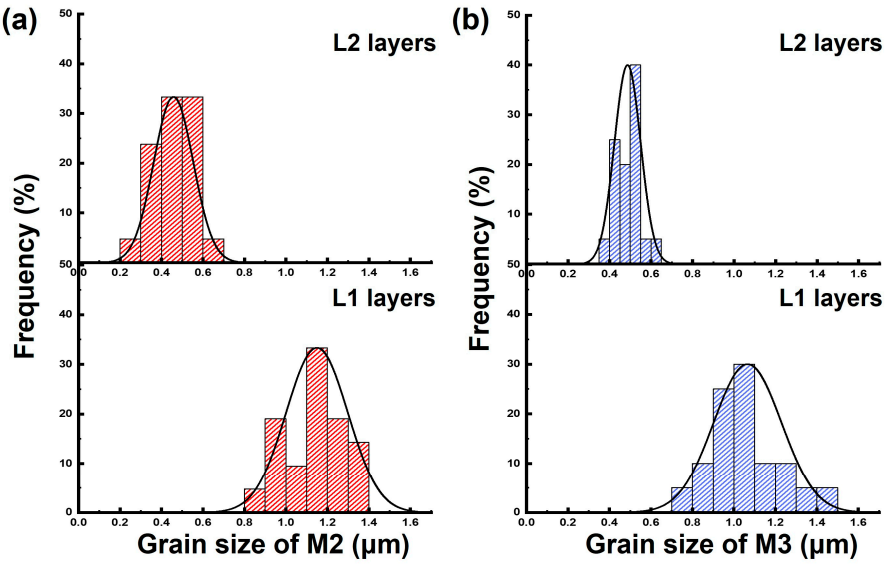


Figure 6. AGS distribution for the (**a**) M2 and the (**b**) M3 samples.

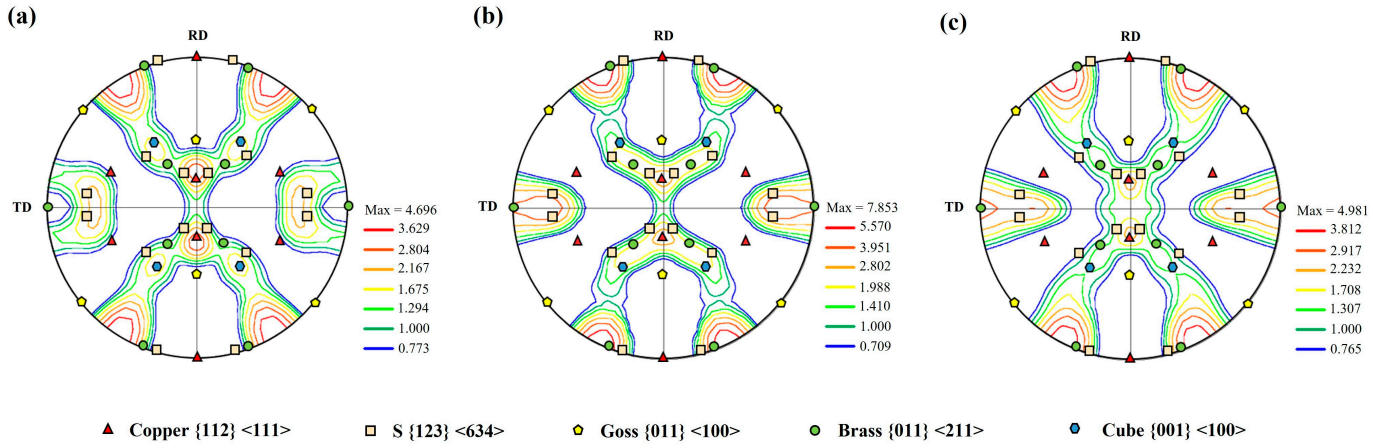


Figure 7. {111} pole figures for the (**a**) M1, (**b**) M2 and (**c**) M3 samples after three MARB cycles.

Figure 8 shows the orientation distribution function (ODF) of the M1 (Figure 8a), M2 (Figure 8b) and M3 (Figure 8c) samples after three MARB cycles were analyzed by EBSD data. There were some components that partially overlap in the PFs [32]. ODF can be used for quantitative analysis about the change in texture during the MARB process. The ideal orientation positions for the typical texture of a face-centered cubic (FCC) crystal are indicated in Figure 7d [33]. It shows that the M2 and M3 samples exhibit a sharper texture component than that of M1. Textural components of M1 (Figure 8a) were Brass {011} <211>, S {123} <634> and Cube {001} <100> with maximum intensity of 5.4 × R, 4.1 × R and 0.7 × R. The development of Brass {011} <211>, S {123} <634>, Copper {112} <111> and Goss {011} <100> components with intensity of 10.8 × R, 4 × R, 1.9 × R and 0.6 × R were analyzed in the ODF for the M2 samples (Figure 8b). Additionally, in the M3 samples (Figure 8c), the maximum intensity of S {123} <634>, Brass {011} <211>, Cube {001} <100> and Copper {112} <111> were 4.6 × R, 2.5 × R, 0.8 × R and 0.6 × R, respectively.

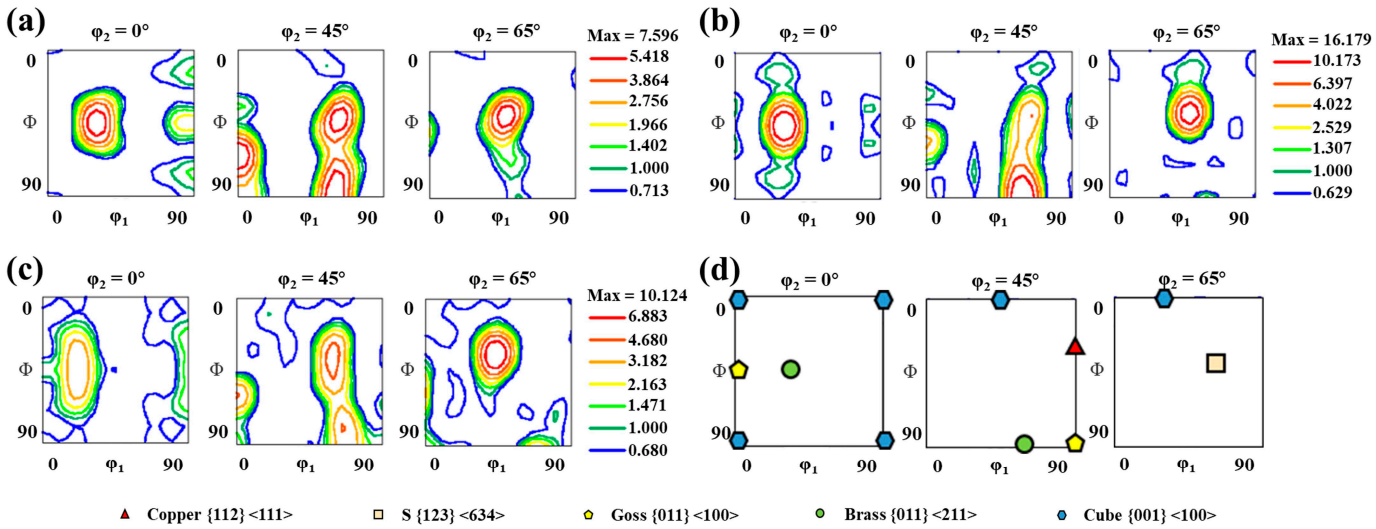


Figure 8. Orientation distribution function for φ2 = 0°, 45° and 65° in (**a**) M1, (**b**) M2, (**c**) M3 after three MARB cycles, and (**d**) ideal positions for typical texture of FCC crystals.

3.2. Mechanical Properties

Figure 9 illustrates the engineering stress–strain curves for M1 (Figure 9a), M2 (Figure 9b) and M3 (Figure 9c) after different cycles. Table 2 provides details for other comparable composites used in the research [34–37]. It is clear that the bimodal Al-SiC composite prepared by the MARB process was more than other samples in strength and elongation. Annealed Al had a low strength (78 MPa) but a high elongation (47%). After the third MARB cycle, a bimodal Al-SiC composite with high strength (225 MPa) and elongation (13%) (Figure 9c) was developed. After the fourth cycle, the TS and elongation of the M3 composites decreased in different degrees (Figure 9c). Compared with M1 after three cycles, the strength and elongation of the M3 samples improved by 23.2% and 7.4% (Figure 9a,c). Compared with M2, the tensile strength of the M3 sample increased by 17.6%, but the elongation decreased by 6.1% (Figure 9b,c). The overall performance of M3 reached a fine balance between strength and ductility after three cycles (Figure 9c).

Table 2. Summary of mechanical properties reported by similar research.

Materials	Number of Cycles	Average Size of Particles (μm)	TS (MPa)	Elongation (%)	Reference
Al-0.5 vol%SiC	7	0.05	140	8	[34]
Al-0.5 vol%SiC/WO_3	7	0.05	180	6	[34]
Al-1 vol%SiC	5	5	220	8	[35]
Al-1 vol%SiC	6	5	205	11	[36]
Al-1.6 vol%SiC	8	7.5	210	7	[37]

Figure 10 shows the microhardness profile for M1, M2 and M3 after different cycles. Each specimen's hardness was tested from the center to the surface of the RD–ND plane. For each sample, a minimum of five measurements were made. A greater than 40% increase was estimated for the three samples after only the first MARB cycle, and the hardness improvement for the M3 samples could reach about 52%. The microhardness improved continually from the second to the fourth cycle. The hardness growth trend slowed down as the number of cycles increased. The microhardness performance of the M2 and M3 groups with bimodal structure were higher than that for the M1 group. The addition of micron-sized SiC particles effectively improved the hardness of the material, so the M3 samples showed the best hardness performance after each cycle.

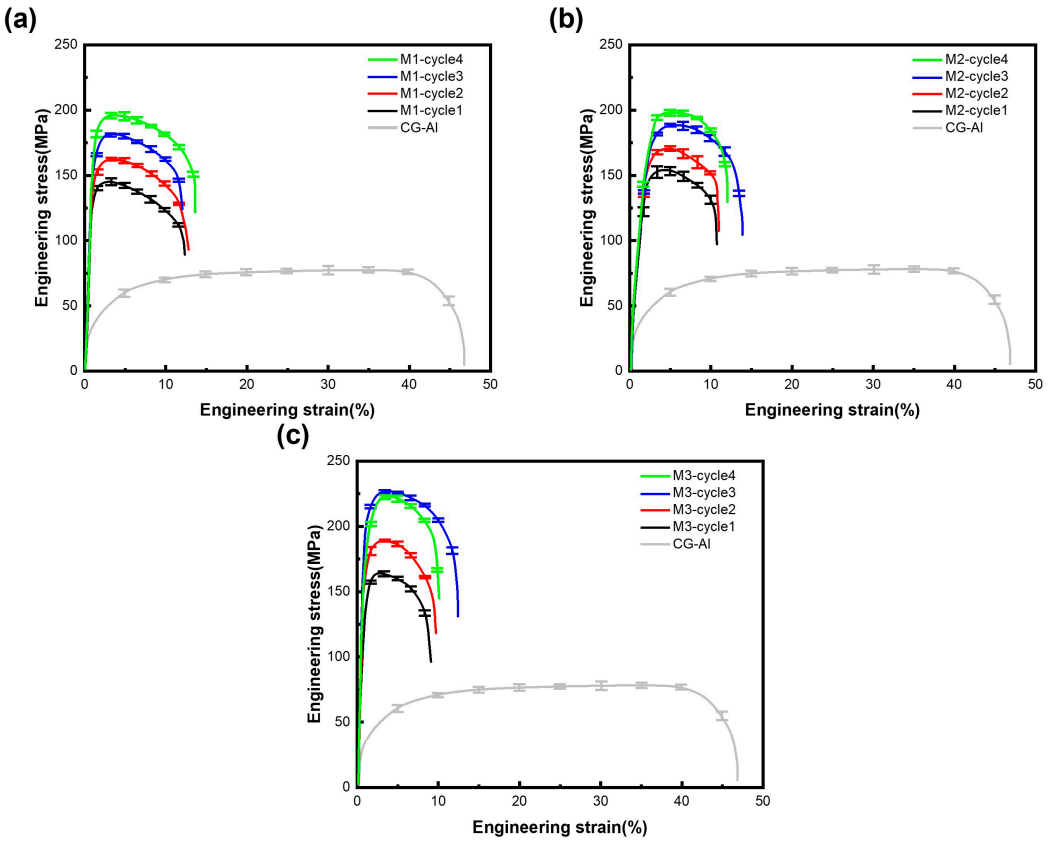


Figure 9. Diagram showing the engineering stress–strain for (**a**) M1, (**b**) M2 and (**c**) M3 after different cycles of MARB.

3.3. Fractography

Figure 11 shows the SEM images of fracture surfaces in M1 (Figure 11a,b), M2 (Figure 11c,d) and M3 (Figure 11e,f) after three cycles. It was observed that all samples had typical ductile fractures characterized by equiaxed fine dimples, which existed in the longitudinal interfaces. Ductile fractures were the result of nucleation, growth and agglomeration of cracks or micropores [25]. Some micropores were observed at the fracture interface that was formed by the gradual peeling of the bonding interface during the tensile process (Figure 11a,c,e). In the bonding interface of the M3 samples with hard-phase particles, micron-sized SiC particles were uniformly distributed between the layers (Figure 11e,f).

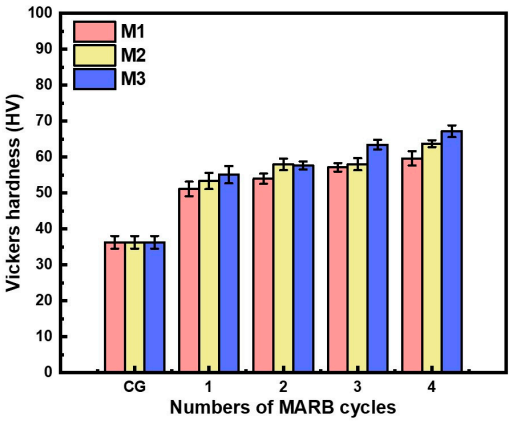


Figure 10. The hardness of M1, M2 and M3.

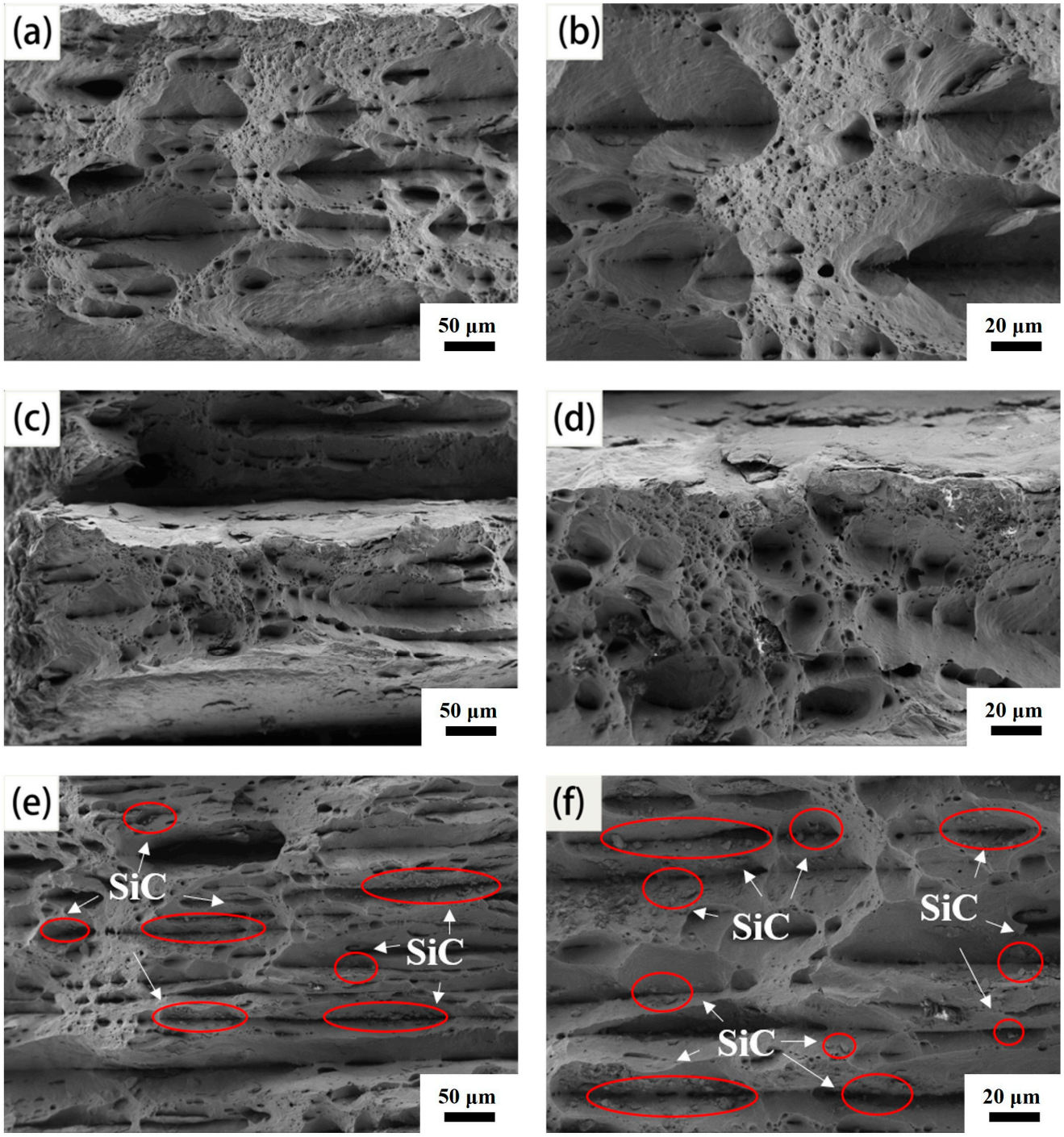


Figure 11. SEM micrographs of the fracture surfaces for the (**a**,**b**) M1, (**c**,**d**) M2, and (**e**,**f**) M3 samples after three MARB cycles.

4. Discussion

4.1. Microstructure Evolution

Alizdeh et al. [20] studied the effects of carbide particles on the bonding strength of aluminum sheets. The results showed that SiC particles decreased the bonding area and strength of the composites. The successful surface bonding of the material requires 50% (without SiC) and 66% (with SiC) reduction in the ARB process. The total reduction for a single cycle in the MARB process was 75% (Figure 2), which can break the limitation of 50% reductions during the traditional ARB process. Compared to the ARB process, there is stronger and tighter bonding at surfaces and interfaces because of a larger deformation

in a single cycle of the MARB process. It was difficult to identify the number of layers in the M3 samples (Figure 4a) after several cycles. With increasing numbers of MARB cycles, micro-sized SiC particles dispersed from the interfaces to the bulk of the aluminum layers (Figure 4). In other words, the MARB process promoted the disappearance of the discontinuity in the interface and the uniform distribution of SiC particles in the aluminum matrix.

Tsuji et al. [29] found that 1100 Al and IF steel with an average thickness greater than 1 μm had obviously localized deformation and high elongation (>30%). However, it was a sudden drop in uniform elongation and total elongation while the grain size was less than 1 μm. In order to control the thickness of the grains in ND, the samples used in abovementioned study were annealed at different temperatures for a fixed time after the ARB process. The samples of the MARB process were annealed in a cycle to control the thickness. The AGS of the L1 layer in the M2 and M3 samples was more than 1 μm after three MARB cycles, while that of the L2 layer was less than 1 μm (Figures 5 and 6). The AGS in ND (thickness) indicated that Al-SiC composites with a bimodal grain structure had been prepared. The embedded larger grains of the L1 layer stabilized the localized deformation and increased the elongation, and grains of the L2 layer maintained strength [25].

The process of surface preparation, cutting, roll-bonding and preheating made the textual evolution of the microstructure more complicated [32]. The deformation mode of the MARB process is a complex combination of plane-strain deformation and redundant shear [38]. Textures in the M1 samples (Figures 7a and 8a) comprised Brass {011} <211>, S {123} <634> and Cube {001} <100>, which was similar to that of rolled aluminum sheets. In the M2 samples (Figures 6b and 7b) with bimodal structure, Brass {011} <211> and S {123} <634> components were developed as the main texture components, while the Cube {001} <100> component decreased and even disappeared.

In low plane-strain deformation of FCC materials, texture deformation orientations develop uniformly along the α-fiber and β-fiber [39,40]. With increasing strain deformation, the β-fiber becomes stronger. The intensity of the Brass {011} <211>, S {123} <634> and Goss {011} <100> texture components along the β-fiber mainly depend on the degree of deformation. The intensity of the S {123} <634> and Brass {011} <211> components in the M3 and M2 samples (Figure 7b,c) with L2 layers was stronger than that in the M1 samples. However, the Brass component decreased in the alloys with added particles [32,39]. Grains in the periphery of SiC particles had different texture orientations and components than others during the MARB process. The strongest orientation of the M3 samples (Figure 8c) was S {123} <634> texture component. The S {123} <634> and Brass {011} <211> texture components decreased in M3 sample compared with that of M2 sample. It is clear that the weak texture components existed such as Cube {001} <100> and Copper {112} <111> in the M3 samples.

The recrystallization texture of the three samples mainly consists of Cube {001} <100> and Goss {011} <100>. Wang et al. [41] found that the particle-stimulated nucleation effect should be the recrystallization mechanism during the Cube {011} <100> orientations formed in the alloy, while the formation of the Goss {011} <100> texture component could be attributed to the nucleation at shear bands. The recrystallization mechanism of the M1 and M3 samples was the particle-stimulated nucleation effect and that of the M2 sample was nucleation at the shear bands. The main texture component of the three samples was Brass {123} <634>. Zhao et al. [42] have revealed that the fracture crack easily penetrated through the Brass grains and the grains closed to the orientation, while the Goss grains were able to facilitate crack deflection. The Goss grains, demonstrating their ability to retard propagation in the M2 sample, may be a profitable factor for its high elongation.

4.2. Mechanical Properties

Strain hardening, grain refining, precipitation hardening and solid solution hardening are the main mechanisms to improve metal strength. In pure aluminum processed by MARB, strain hardening and grain refining are the major strengthening mechanisms.

The strength increased by 90.7%, 97.7% and 112.5% after the first MARB cycle (Figure 9) compared with annealed plates. Higher improvement in the strength of the M2 (Figure 9b) compared with M1 (Figure 9c) was due to more strain hardening in the L2 layer. In addition to the aforementioned mechanisms, dispersion of particles was also one important mechanism in the M3 samples [43]. Yield and tensile strength greatly increased from the second to third MARB cycle and then increased slightly from the third to fourth cycle. After three MARB cycles, the tensile strength of the M3 group (Figure 9c) was about 1.23 times higher than that of the M1 group. Saturation was observed in the strength after four MARB cycles, and tensile strength increased by 8.5%, 5% and −0.53% (M1 to M3 samples) compared with that of the third-cycle samples. With an increasing number of layers, the number of bonding interfaces caused a limited reduction in tensile strength [44].

According to Figure 8, the elongation of the three sample groups gradually increased in the first three cycles. The grain size of the L1 and L2 layers (Figure 5) was about 1.07 and 0.48 μm after three MARB cycles. Elongated coarse grains in the L1 layer have a greater ability to accumulate dislocations, which can increase the uniform elongation and achieve reasonable ductility [25]. Elongation of the M2 and M3 samples after three cycles increased by 14% and 7.4% compared with that for the M1 specimen (Figure 9). Non-uniform distribution of SiC particles, reduction in bonding area and presence of porosities were the main reason for the decrease in the ductility of the M3 composites. As grain size decreased after four MARB cycles, the elongation of M2 and M3 with bimodal structure had different degrees of reduction (Figure 9). The Al-SiC composites produced by MARB achieved the best match of strength and plasticity after three cycles.

The hardness of the M1, M2 and M3 samples increased with variation in the number of cycles (Figure 9). Microhardness of the bimodal structure material was higher in all cycles than that for the M1 sample prepared by the conventional MARB process. The average hardness of the M3 sample reached 63 and 67 HV after the third and fourth cycle. Dispersion of SiC particles and adequate bonding between the layers as the number of cycles increased promoted an improvement in strength, ductility and hardness (Figure 4). The content of SiC particles per unit area was also an important factor affecting the microhardness of the Al-SiC composites.

4.3. Fractography

The fracture surfaces after the tensile test of all the samples exhibited a typical ductile fracture with different features and morphologies (Figure 11). Ductile fracture occurred with three stages: nucleation of cracks or cavities, growth with continued deformation, and coalescence until complete rupture [45]. Significant deformation and necking occurred during the tensile test. The failure of the M1 and M2 samples (Figure 11b,d) was influenced by shear stress, and the bonding interfaces tended to form curved depressions. The dimples at the bonding longitudinal interfaces of the M1 sample (Figure 11b) were equiaxed and fine, while those of the M2 sample (Figure 11d) were equiaxed, hemispherical and deep. The overall appearance of the dimples in the M2 samples in the bonding longitudinal interfaces were similar to honeycomb, which was related to the high elongation exhibited in the tensile tests. Ductile fracture of M3 (Figure 11f) was characterized by acicular dimple and circular micropores.

In the Al-SiC composite, voids and cracks nucleated and grew in the aluminum matrix and Al/SiC interface (Figure 11f). Comparing the dimples that formed among the particles with others, the former were larger and deeper than the latter. The overall features of ductile fracture were determined by the size, number and distribution of the particles in the bonding interfaces. Elongation of the M3 samples (Figure 9) was lower than that of for M2, perhaps the result of the addition of micron-sized reinforcing-phase particles (Figure 11f).

5. Conclusions

In this paper, a study was conducted on the evolution of microstructure, crystallographic texture and mechanical properties of Al-SiC composites with bimodal structure,

as prepared with 1050 Al. Additionally, a comparison was performed between samples M1, M2 and M3. The evolution process was analyzed by SEM, EBSD and tensile test. The following conclusions were drawn from this study:

(1) Grain size less than and greater than 1 μm bimodal Al-SiC composite with high strength (225 MPa) and elongation (13%) was obtained. The bimodal MMCs reached a reasonable balance between strength and ductility.
(2) The AGS in the ND for the L1 layers of samples M1, M2 and M3 were 0.92, 1.15 and 1.07 μm, while that for the L2 layers of M2 and M3 were 0.46 and 0.48 μm after three MARB cycles. The grain size was controlled by intermediate annealing during one MARB cycle.
(3) The texture components of the M3 samples consisted of S {123} <634>, Brass {011} <211>, Cube {001} <100> and Copper {112} <111>. The texture components of the M1 were Brass {011} <211>, S {123} <634> and Cube {001} <100>. Brass {011} <211>, S {123} <634>, Copper {112} <111> and Goss {011} <100> components were analyzed in the M2 samples. The differences in the three samples caused the variation in the texture components.
(4) With an increasing number of layers, the number of bonding interfaces caused a limited reduction in tensile strength. Strength saturation was observed in the M3 samples after four MARB cycles.
(5) All samples conformed to ductile fracture with an equiaxed dimple. Dimples in the M1 sample were fine and equiaxed. Honeycomb, equiaxed and deep dimples were found in M2. The morphology of M3 was mainly acicular dimples and circular micropores along the SiC particles.

Author Contributions: Conceptualization, S.Z.; Methodology, S.Z.; Validation, B.F.; Formal analysis, B.F.; Investigation, B.F.; Writing—original draft, S.Z.; Writing—review & editing, Y.G.; Project administration, L.W.; Funding acquisition, L.W. All authors have read and agreed to the published version of the manuscript.

Funding: This research was funded by Shanghai Metallurgical Technology and Equipment Detection Service Platform, grant number 11 DZ2291200.

Institutional Review Board Statement: Not applicable.

Informed Consent Statement: Not applicable.

Data Availability Statement: The data that support the findings of this study are available from the corresponding author upon reasonable request.

Conflicts of Interest: The authors declare no conflict of interest.

References

1. Wang, Y.; Zhang, S.; Wu, R.; Turakhodjaev, N.; Zhang, J.; Liu, M.; Mardonakulov, S. Concurrently improving uniform elongation and strength of ultrafine-grained Al–2Li alloy. *Mater. Sci. Eng. A* **2020**, *792*, 139848. [CrossRef]
2. Ivanov, K.V.; Ovcharenko, V.E. Structural features of ultrafine-grained aluminum processed through accumulative roll bonding providing improved mechanical properties and thermal stability. *Mater. Sci. Eng. A* **2020**, *775*, 138988. [CrossRef]
3. Etemad, A.; Dini, G.; Schwarz, S. Accumulative roll bonding (ARB)-processed high-manganese twinning induced plasticity (TWIP) steel with extraordinary strength and reasonable ductility. *Mater. Sci. Eng. A* **2019**, *742*, 27–32. [CrossRef]
4. Wang, M.; Lv, H.; Zhang, C.; Li, M.; Gao, H.; Wang, J.; Sun, B. High strength high electrical conductivity ultrafine-grained Al–Y alloy processed via cold drawing. *Mater. Sci. Eng. A* **2020**, *772*, 138824. [CrossRef]
5. Feng, Z.; Hu, H.; Wang, J.; Dong, H.; Zhang, X.; Ma, J.; Wang, J.; Liu, D.; Li, J.; Zhang, X. Revealing the evolution mechanisms of microstructure, texture and mechanical behavior in Zr702 alloy plates fabricated by accumulative roll bonding. *Mater. Sci. Eng. A* **2023**, *864*, 144609. [CrossRef]
6. Xu, R.; Liang, N.; Zhuang, L.; Wei, D.; Zhao, Y. Microstructure and mechanical behaviors of Al/Cu laminated composites fabricated by accumulative roll bonding and intermediate annealing. *Mater. Sci. Eng. A* **2022**, *832*, 142510. [CrossRef]
7. Ebrahimi, M.; Wang, Q. Accumulative roll-bonding of aluminum alloys and composites: An overview of properties and performance. *J. Mater. Res. Technol.* **2022**, *19*, 4381–4403. [CrossRef]

8. Wang, Y.; Zhong, F.; Wu, R.; Wu, H.; Turakhodjaev, N.; Kudratkhon, B.; Sun, J.; Hou, L.; Zhang, J.; Li, X.; et al. High-strength, ductility and modulus Al–Li/B_4C composite with near nanostructure produced by accumulative roll bonding. *J. Alloys Compd.* **2020**, *834*, 155105. [CrossRef]
9. Alawadhi, M.Y.; Sabbaghianrad, S.; Huang, Y.; Langdon, T.G. Evaluating the paradox of strength and ductility in ultrafine-grained oxygen-free copper processed by ECAP at room temperature. *Mater. Sci. Eng. A* **2021**, *802*, 140546. [CrossRef]
10. Jang, G.; Kim, J.N.; Lee, H.; Lee, T.; Enikeev, N.; Abramova, M.; Valiev, R.Z.; Kim, H.S.; Lee, C.S. Microstructural evolution and mechanical properties of nanocrystalline Fe–Mn–Al–C steel processed by high-pressure torsion. *Mater. Sci. Eng. A* **2021**, *827*, 142073.
11. Bazarnik, P.; Bartkowska, A.; Huang, Y.; Szlązak, K.; Adamczyk-Cieślak, B.; Sort, J.; Lewandowska, M.; Langdon, T.G. Fabrication of hybrid nanocrystalline Al–Ti alloys by mechanical bonding through high-pressure torsion. *Mater. Sci. Eng. A* **2022**, *833*, 142549. [CrossRef]
12. Saito, Y.; Utsunomiya, H.; Tsuji, N.; Sakai, T. Novel ultra-high straining process for bulk materials—Development of the accumulative roll-bonding (ARB) process. *Acta Mater.* **1999**, *47*, 579–583. [CrossRef]
13. Kümmel, F.; Diepold, B.; Sauer, K.F.; Schunk, C.; Prakash, A.; Höppel, H.W.; Göken, M. High Lightweight Potential of Ultrafine-Grained Aluminum/Steel Laminated Metal Composites Produced by Accumulative Roll Bonding. *Adv. Eng. Mater.* **2019**, *21*, 1800286. [CrossRef]
14. Ostolaza, M.; Arrizubieta, J.I.; Queguineur, A.; Valtonen, K.; Lamikiz, A.; Ituarte, I.F. Influence of process parameters on the particle–matrix interaction of WC-Co metal matrix composites produced by laser-directed energy deposition. *Mater. Des.* **2022**, *223*, 111172. [CrossRef]
15. Shalnova, S.A.; Volosevich, D.V.; Sannikov, M.I.; Magidov, I.S.; Mikhaylovskiy, K.V.; Turichin, G.A.; Klimova-Korsmik, O.G. Direct energy deposition of SiC reinforced Ti–6Al–4V metal matrix composites: Structure and mechanical properties. *Ceram. Int.* **2022**, *48*, 35076–35084. [CrossRef]
16. Wu, H.; Xu, W.; Shan, D.; Wang, X.; Guo, B.; Jin, B.C. Micromechanical modeling of damage evolution and fracture behavior in particle reinforced metal matrix composites based on the conventional theory of mechanism-based strain gradient plasticity. *J. Mater. Res. Technol.* **2023**, *22*, 625–641. [CrossRef]
17. Zhang, Y.; Yu, Y.; Wang, L.; Li, Y.; Lin, F.; Yan, W. Dispersion of reinforcing micro-particles in the powder bed fusion additive manufacturing of metal matrix composites. *Acta Mater.* **2022**, *235*, 118086. [CrossRef]
18. He, H.; Fan, G.; Saba, F.; Tan, Z.; Su, Z.; Xiong, D.; Li, Z. Enhanced distribution and mechanical properties of high content nanoparticles reinforced metal matrix composite prepared by flake dispersion. *Composites Part B* **2023**, *252*, 110514. [CrossRef]
19. Ghalehbandi, S.M.; Malaki, M.; Gupta, M. Accumulative Roll Bonding—A Review. *Appl. Sci.* **2019**, *9*, 3627. [CrossRef]
20. Alizadeh, M.; Paydar, M.H. Fabrication of Al/SiC_P composite strips by repeated roll-bonding (RRB) process. *J. Alloys Compd.* **2009**, *477*, 811–816. [CrossRef]
21. Zheng, H.; Wu, R.; Hou, L.; Zhang, J.; Zhang, M. Mathematical analysis and its experimental comparisons for the accumulative roll bonding (ARB) process with different superimposed layers. *J. Magn. Alloys* **2021**, *9*, 1741–1752. [CrossRef]
22. Xu, R.; Tang, D.; Ren, X.; Wen, X.; Wen, Y. Improvement of the matrix and the interface quality of a Cu/Al composite by the MARB process. *Rare Met.* **2007**, *26*, 230–235. [CrossRef]
23. Lu, K. Making strong nanomaterials ductile with gradients. *Science* **2014**, *345*, 1455–1456. [CrossRef] [PubMed]
24. Li, R.; Ding, Y.; Zhang, H.; Lei, J.; Shen, Y. Effective strengthening and toughening in Zn–1Mg alloy with bimodal grain structure achieved by conventional extrusion. *Mater. Sci. Eng. A* **2022**, *854*, 143850. [CrossRef]
25. Naseri, M.; Reihanian, M.; Borhani, E. A new strategy to simultaneous increase in the strength and ductility of AA2024 alloy via accumulative roll bonding (ARB). *Mater. Sci. Eng. A* **2016**, *656*, 12–20. [CrossRef]
26. Wang, Y.M.; Ma, E. Three strategies to achieve uniform tensile deformation in a nanostructured metal. *Acta Mater.* **2004**, *52*, 1699–1709. [CrossRef]
27. Wu, X.; Yang, M.; Yuan, F.; Wu, G.; Wei, Y.; Huang, X.; Zhu, Y. Heterogeneous lamella structure unites ultrafine-grain strength with coarse-grain ductility. *Proc. Natl. Acad. Sci. USA* **2015**, *112*, 14501–14505. [CrossRef] [PubMed]
28. Hosseiny, N.; Shabani, A.; Toroghinejad, M.R. Effect of bimodal microstructure on texture evolution and mechanical proper-ties of 1050 Al alloy processed through severe plastic deformation and subsequent annealing. *Mater. Sci. Eng. A* **2021**, *82*, 141580. [CrossRef]
29. Tsuji, N.; Ito, Y.; Saito, Y.; Minamino, M. Strength and ductility of ultrafine grained aluminum and iron produced by ARB and annealing. *Scr. Mater.* **2002**, *47*, 893–899. [CrossRef]
30. Azad, B.; Borhani, E. Pre-aging time dependence of microstructure and mechanical properties in nanostructured Al-2wt% Cu alloy. *Met. Mater. Int.* **2016**, *22*, 243–251. [CrossRef]
31. Sarvi, Z.; Sadeghi, A.; Mashhadi, M.M.; Guo, B. Effect of Accumulative Roll Bonding (ARB) strain path on microstructural evolution and crystallographic texture development in aluminium. *J. Mater. Res. Technol.* **2022**, *21*, 1061–1071. [CrossRef]
32. Naseri, M.; Reihanian, M.; Borhani, E. Effect of strain path on microstructure, deformation texture and mechanical properties of nano/ultrafine grained AA1050 processed by accumulative roll bonding (ARB). *Mater. Sci. Eng. A* **2016**, *673*, 288–298. [CrossRef]
33. Borhani, E.; Jafarian, H.; Shibata, A.; Tsuji, N. Texture evolution in Al–0.2 mass% Sc alloy during ARB process and subsequent annealing. *Mater. Trans.* **2012**, *53*, 72–80. [CrossRef]

34. Baazamat, S.; Tajally, M.; Borhani, E. Fabrication and characteristic of Al-based hybrid nanocomposite reinforced with WO3 and SiC by accumulative roll bonding process. *J. Alloys Compd.* **2015**, *653*, 39–46. [CrossRef]
35. Khdair, A.I.; Fathy, A. Enhanced strength and ductility of Al-SiC nanocomposites synthesized by accumulative roll bonding. *J. Mater. Res. Technol.* **2020**, *9*, 478–489. [CrossRef]
36. Alizadeh, M.; Paydar, M.H. Fabrication of nanostructure Al/SiC_P composite by accumulative roll-bonding (ARB) process. *J. Alloys Compd.* **2010**, *492*, 231–235. [CrossRef]
37. Reihanian, M.; Fayezipour, S.; Lari Baghal, S.M. Nanostructured Al/SiC-graphite composites produced by accumulative roll bonding: Role of graphite on microstructure, wear and tensile behavior. *J. Mater. Eng. Perform.* **2017**, *26*, 1908–1919. [CrossRef]
38. Kamikawa, N.; Tsuji, N.; Minamino, Y. Microstructure and texture through thickness of ultralow carbon IF steel sheet severely deformed by accumulative roll-bonding. *Sci. Technol. Adv. Mater.* **2004**, *5*, 163. [CrossRef]
39. Quadir, M.Z.; Ferry, M.; Al-Buhamad, O.; Munroe, P.R. Shear banding and recrystallization texture development in a multilayered Al alloy sheet produced by accumulative roll bonding. *Acta Mater.* **2009**, *57*, 29–40. [CrossRef]
40. Chowdhury, S.G.; Dutta, A.; Ravikumar, B.; Kumar, A. Textural evolution during accumulative roll bonding of an Al–Li alloy. *Mater. Sci. Eng. A* **2006**, *428*, 351–357. [CrossRef]
41. Wang, X.; Guo, M.; Chapuis, A.; Luo, J.; Zhang, J.; Zhuang, L. The dependence of final microstructure, texture evolution and mechanical properties of Al–Mg–Si–Cu alloy sheets on the intermediate annealing. *Mater. Sci. Eng. A* **2015**, *633*, 46–58. [CrossRef]
42. Zhao, Q.; Liu, Z.; Huang, T.; Xia, P.; Li, F. Enhanced fracture toughness in an annealed Al-Cu-Mg alloy by increasing Goss/Brass texture ratio. *Mater. Charact.* **2016**, *119*, 47–54. [CrossRef]
43. Reihanian, M.; Hadadian, F.K.; Paydar, M.H. Fabrication of Al–2vol%Al_2O_3/SiC hybrid composite via accumulative roll bonding (ARB): An investigation of the microstructure and mechanical properties. *Mater. Sci. Eng. A* **2014**, *607*, 188–196. [CrossRef]
44. Attar, A.A.; Nia, A.A.; Mazaheri, Y.; Ghassemali, E. High Strength-Elongation Balance in Warm Accumulative Roll Bonded AA1050 Sheets. *Met. Mater. Int.* **2022**, *28*, 346–360. [CrossRef]
45. Stone, R.V.; Cox, T.B.; Low, J.R.; Psioda, J.A. Microstructural aspects of fracture by dimpled rupture. *Int. Met. Rev.* **1985**, *30*, 157–180. [CrossRef]

Disclaimer/Publisher's Note: The statements, opinions and data contained in all publications are solely those of the individual author(s) and contributor(s) and not of MDPI and/or the editor(s). MDPI and/or the editor(s) disclaim responsibility for any injury to people or property resulting from any ideas, methods, instructions or products referred to in the content.